

Supplementary information

Label-free detection and profiling of individual solution-phase molecules

In the format provided by the authors and unedited

Supplementary Materials for

Label-free detection and profiling of individual solution-phase molecules

Lisa-Maria Needham, Carlos Saavedra, Julia K. Rasch, Daniel Sole-Barber, Beau S. Schweitzer, Alex J. Fairhall, Cecilia H. Vollbrecht, Sushu Wan, Yulia Podorova, Anders J. Bergsten, Brandon Mehlenbacher, Zhao Zhang, Lukas Tenbrake, Jovanna Saimi, Lucy C. Kneely, Jackson S. Kirkwood, Hannes Pfeifer, Edwin R. Chapman,
Randall H. Goldsmith*


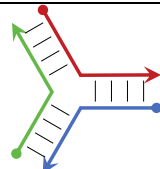
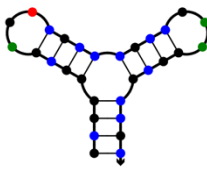
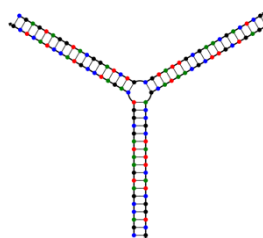
*Corresponding author. Email: rhg@chem.wisc.edu (R.H.G.)

Table of Contents

DNA Samples	3
Simulations and calculations	4
Calculated resonance shift.....	4
Molecular velocity distributions and molecular mean-square-displacement power- spectral-density.....	7
Simulated photothermal bandwidth determination.....	8
Fiber Cavity Mechanics.....	10
Additional Discussion	13
Navigating Surface Effects in Single-Molecule Studies	13
Limitations of our Approach, Context, and Future Directions.....	15
Supplementary Figures and Tables	19
Supplementary references	34

DNA Samples

Table S 1. DNA structures and sequences

Structure	Sequence	Molecular weight (kDa)
	TGGAGAGAATCGGTCACAGTACAACCG CGGTTGTA CTGTGACCGATTCTCTCCA	16.6
	TGGAGAGAATCGGTCACA GTACAACCGTTCTCTCCA TGTGACCGACGGTTGTAC	16.6
	GCGGGGCGAGTCGCCCGCCGAAGGCGCCGC	9.3
	CGACCGATGAATAGCGGTCAGATCCGTACCTACTCG CGAGTCGTTTCGCAATACGACCGCTATTCATCGGTCG CGAGTAGGTACGGATCTGCGTATTGCGAACGACTCG	33.3

Simulations and calculations

Calculated resonance shift

We can use analytical expressions to determine frequency shifts from small objects¹⁻³. Essentially, these are the shifts induced without any additional photothermal enhancements, and can be thought of as the observed shifts in cavities with extremely small circulating power. We used two approaches, first we applied Equation 1 following the approach by Kohler *et al*⁴ (Figure S 13). Here, the polarizability of the molecule is calculated via the Lorentz-Lorenz equation, Equation 2, for mixtures weighted by the overlap between the mode volume and the molecule and divided by the volume of the molecule:

$$\langle \alpha \rangle = \frac{\alpha}{V_{mol}} \int_{V_{mol}} dV_{np} \left(\frac{\omega_0}{\omega(z)} \right) \exp \frac{-2(x^2 + y^2)}{\omega(z)^2} \cos^2(kz) \quad \text{Equation 1}$$

where

$$\alpha = 4\pi r^3 \epsilon_0 \frac{n_{mol}^2 - n_{water}^2}{n_{mol}^2 + 2n_{water}^2} \quad \text{Equation 2}$$

$$\omega(z) = \frac{\omega_0}{\sqrt{1 + \left(\frac{z}{z_0}\right)^2}} \quad \text{Equation 3}$$

The mode area and the Rayleigh length are:

$$\omega_0^2 = \frac{L\lambda_m}{\pi} \sqrt{\frac{G_1 G_2 (1 - G_1 G_2)}{(G_1 + G_2 - 2G_1 G_2)^2}} \quad \text{Equation 4}$$

$$z_0 = \pi \omega_0^2 / \lambda_m \quad \text{Equation 5}$$

correspondingly. Here L is the cavity length, $\lambda_m = \lambda_0/n_{water}$ is the wavelength in the medium, and the cavity geometry parameters are $G_i = 1 - L/R_i$, where R_i are the radius of curvature of each mirror. The cavity frequency shift is:

$$\Delta\nu = \frac{\langle \alpha \rangle c}{2\lambda_m \epsilon_0 V_{mode}} \quad \text{Equation 6}$$

where c is the speed of light in vacuum and the mode volume is $V_{mode} = \pi \omega_0^2 L / 4$. This approach differs from Kohler *et al*⁴ as the molecules are significantly smaller than the mode

volume and therefore the mode shape shifts a negligible amount on the length scale of the molecule.

For the four proteins interrogated in this work the corresponding resonance shifts ($\Delta\nu$) that would be induced by interaction with the cavity mode were calculated (Table S 2).

Table S 2. Calculated resonance shifts induced by proteins streptavidin, carbonic anhydrase, aprotinin and Myc-tag upon interaction with the mode volume of the FP microcavity. This approach was taken from Kohler *et al*⁴.

Protein	Refractive index	Protein radius (nm)	$\Delta\nu$ (kHz)
Streptavidin	1.43	2.80	49.0
Carbonic anhydrase	1.43	2.10	21.0
Aprotinin	1.43	1.45	6.7
Myc-tag	1.43	0.75	0.96

The second approach was adapted from Su *et al*⁵. First, the polarizability was calculated as previously shown using Equation 1. The wavelength shift was then calculated following Equation 7:

$$\Delta\lambda_{max} = \frac{\langle\alpha\rangle \left[\frac{E_0^2(r_e)}{E_{max}^2} \right]}{2V_m} \lambda \quad \text{Equation 7}$$

where r was the particle radius, λ the free space wavelength, $\frac{E_0^2(r_e)}{E_{max}^2}$ was calculated to be 1/5.5 for the microtoroid⁵ and 1/4.8 for the FP microcavity, since the molecule is able to overlap with the mode maximum. To calculate the resonance shift expected from interaction of the proteins with a toroidal microresonator the mode volume, V_m , was taken from Su *et al*⁵ and was equal to 330 μm^3 . In order to compare to the expected resonance shift from the

FP cavities used in this work, V_m was calculated to be $80 \mu\text{m}^3$. Given these values, the resulting frequency shifts were calculated as shown in Table S 3.

Table S 3. Calculated resonance shifts induced by proteins streptavidin, carbonic anhydrase, aprotinin and Myc-tag upon interaction with the optical mode of a toroidal microcavity. This approach compares the calculated shifts given the mode volume of a toroidal microcavity and our FP microcavity and was taken from Su *et al*⁵.

Protein	Refractive index	Protein Radius (nm)	$\Delta\nu$ toroid (kHz)	$\Delta\nu$ FP (kHz)
Streptavidin	1.43	2.80	3.796	15.064
Carbonic anhydrase	1.43	2.10	1.601	6.355
Aprotinin	1.43	1.45	0.530	2.092
Myc-tag	1.43	0.75	0.075	0.297

The magnitude of the resonance shifts induced from the interaction between the proteins and the mode of a toroidal microresonator are less than the shifts from the same interaction in our FP cavities. The confinement of the optical mode in the medium outside of the dielectric material in FP microcavities allows for stronger overlap between the molecule and the mode when compared to a toroid, in which the mode is confined within the dielectric material (Table S 2). Furthermore, the smaller mode volume in the FP microcavity facilitates stronger light-matter interactions further resulting in larger resonance shifts compared to those achieved with a toroidal microcavity (Table S 3).

Molecular velocity distributions and molecular mean-square-displacement power-spectral-density

The velocity distribution of particles undergoing free Brownian motion in solution follow Equation 8 and Equation 9 ⁶:

$$m^* = m_p + \frac{1}{2}m_f \quad \text{Equation 8}$$

$$f(v) = \sqrt{\frac{m^*}{2\pi k_B T}} e^{-\frac{m^* v^2}{2k_B T}} \quad \text{Equation 9}$$

for particle of mass m_p , displaced solution mass m_f , and solution temperature T . An effective mass was calculated in order to include the effects of the solution on the acceleration of the particle. With these equations, one can approximate the likelihood of a particle to move with a given velocity (Figure S 15A). The smaller the particle, the wider the velocity distribution becomes.

The mean squared displacement power spectral density (MSDPSD) of a particle undergoing free Brownian motion can be calculated with the Equation 13 ⁶, derived as a solution to the Langevin equation:

$$D = \frac{k_B T}{6\pi\eta r} \quad \text{Equation 10}$$

$$\tau_f = \frac{r^2 \rho_f}{\eta}, \tau_p = \frac{m}{6\pi\eta r} \quad \text{Equation 11}$$

$$\phi_f = \frac{1}{2\pi\tau_f}, \phi_p = \frac{1}{2\pi\tau_p} \quad \text{Equation 12}$$

$$P_{free}(f) = \frac{D}{\pi^2 f^2} \frac{1 + \sqrt{f/2\phi_f}}{(\sqrt{f/2\phi_f} + f/\phi_p + f/9\phi_f)^2 + (1 + \sqrt{f/2\phi_f})^2} \quad \text{Equation 13}$$

for particle radius r , particle mass m , solution density ρ_f , solution viscosity η , and solution temperature T . The τ terms are time constants, τ_f related to inertia of the surrounding fluid, and τ_p to the inertia of the particle itself. We note that this version of the equation is for a free particle (not confined by an optical trap).

This equation was plotted for the four proteins using known mass and radius values for streptavidin, carbonic anhydrase, and aprotinin, with a calculated radius for Myc-tag (Figure 5A, Figure S 15B). A range from 1 kHz to 1 MHz was plotted in Figure 5a. Integrating over the Molecular Velocity Filter Bandwidth (the window between the high frequency edge of locking bandwidth to the low frequency edge of photothermal bandwidth), from 5 kHz to 21 kHz yields the mean squared displacement of the molecules over this bandwidth, giving $0.00875 \mu\text{m}^2$ for Myc-tag, $0.00457 \mu\text{m}^2$ for aprotinin, $0.00315 \mu\text{m}^2$ for carbonic anhydrase, and $0.00237 \mu\text{m}^2$ for streptavidin. The root mean square (RMS) displacement for streptavidin was considered in the manuscript Discussion as being comparable to the distance between the microcavity node and antinode, thus suggesting that the molecule can diffuse from node to antinode on this timescale. The variation in MSDPSD values among the different proteins reflect differences in their mass and size, which is valuable for understanding the Brownian motion characteristics of the particles and their conformation. In this treatment, convection is neglected. A COMSOL (version 6.0) simulation was carried out to estimate the Rayleigh number (R_a) inside the microcavity at (slightly) elevated temperature. The largest value of R_a was determined to be 1.48×10^{-6} , well below the range where convection is relevant.

Simulated photothermal bandwidth determination

Finite element simulations were performed using COMSOL. The adiabatic model⁷ was used to solve for the stable equilibrium of the cavity resonance frequency/length/wavelength under high circulating power conditions. While the cavity is locked, the heat generated by the absorbed circulating power is dissipated by the heat conduction into the surrounding medium. The cavity equilibrium resonance frequency is determined by the heat conductance of the system (K) (assuming no convection or radiation). The thermal conductance of the system was calculated by considering a volume

of water, equivalent to the optical mode volume, which is heated according to Equation 15. If

a_{water} is the absorbed power in water:

$$a_{water} = \pi \frac{1}{F_{air}} - \frac{1}{F_{water}} \quad \text{Equation 14}$$

where F is the finesse in air/water respectively, the total absorbed power is:

$$P_{abs} = P_{circ} a \quad \text{Equation 15}$$

where, P_{circ} is defined as the circulating cavity power:

$$P_{circ} = P_{in} T \eta \left(\frac{F^2}{\pi^2} \right) \quad \text{Equation 16}$$

$$\eta = |\langle \psi_{cav} | \psi_f \rangle|^2 \approx \frac{4d_m^2 d_f^2}{(d_m^2 + d_f^2)^2} \quad \text{Equation 17}$$

where where P_{in} is the input power,⁸ η is the mode matching overlap integral⁸, $d_m = \omega(z = L/2)$ is the mode radius at fiber mirror (Equation 3), d_f is the radius of the mode inside the SM fiber. T is the transmission factor of the mirror coating (transmission=10 ppm) and F is the cavity finesse. This expression is valid for all cavity systems influenced by absorption losses⁹. Consequently, the total power flow across a gaussian surface surrounding the mode volume of the cavity is measured on a 200 μ s time-scale. This integration time was arbitrarily chosen to be much longer than the measured photothermal time-constant of the system, determined to be 7.57 μ s. Based on the distribution of the optical mode (Extended data Fig 8) for the geometry of cavity one, a cylinder of water with radius 1.25 μ m and length 19 μ m was used as the heat source to the model. A volume of water defined by a sphere (radius 25 μ m) acted as a heat sink for the system. A glass cylinder of diameter 125 μ m was placed tangent to each circular face of the heat source, representing the fibers. Using the Heat Transfer in Solids and Fluids module, a constant power density of 42.2 GW/m³ was applied to the cylinder. This power density was calculated based on the circulating power of the cavity and the absorption of water, giving 3.94 μ W of

absorbed power over the volume of the cylinder. The system was set to an initial temperature of 293.15 K, and was allowed to evolve with this power input, approaching a temperature of 293.28 K.

To estimate the thermal relaxation time, we initialized the system at the equilibrium temperature and studied its characteristic temperature decay profile. The resulting temperature over time data was then fit with an exponential decay curve (Figure S 16B). This yielded a time constant of 7.57 μs , consistent with a thermal bandwidth of 66.05 kHz approximately 3-fold larger than the measured value of 21 kHz (Figure S 16A). This small discrepancy is likely due to non-idealities not considered in the simulation, such as additional contact points with the ferrule which were not considered.

Fiber Cavity Mechanics

Finite element simulations on mechanical fluctuations of the cavity were performed using COMSOL (version 6.0). The fiber cavity was modelled (Figure S 20) including the fibers (glass), ferrule (glass) and piezos (Lead zirconate titanate with Young's Modulus 82.1 GPa and Poisson Ratio 0.39)¹⁰, and glass plate (Figure S 20). The piezos (2.5 mm \times 2.3 mm \times 2.5 mm) sat on top of the glass block (20 mm \times 7 mm \times 3 mm). The slotted ferrule section has the left half (3.4 mm \times 1.25 mm \times 1.25 mm) separated from the right (4.6 mm \times 1.25 mm \times 1.25 mm) by a gap of 125 μm . The bore was placed 0.833 mm from the bottom of the ferrule, with a radius of 65.5 μm . There was a half cut through the right ferrule, 0.5 mm from the full gap between left and right. The fibers were each placed within the bore, approximately tangent to the bottom, with a radius of 125 μm . A 19 μm separation between the fibers defined the optical cavity. The water was modeled as an ellipsoid (1 mm \times 0.6 mm \times 1.25 mm), centered on the plane of the top of the ferrule, directly above the gap between the fibers. The parts of this ellipsoid clipping with the fibers and ferrule were removed. The two modules used for this simulation were Solid Mechanics for all the glass components and piezos, and Pressure Acoustics, Frequency Domain for the water components. Multiphysics

boundaries between the two were included. The eigenfrequencies and eigenmodes of this system both with and without water were calculated. Eigenmodes appearing in both the air and water simulations were used for further calculations.

The noise spectral density was calculated as previously described ¹¹. From the simulations, the effective masses of the eigenmodes are first calculated, following the equation:

$$m_{eff} = \frac{\int_V dV \rho(x, y, z) \cdot |\mathbf{u}(x, y, z)|^2}{\max_V (|\mathbf{u}(x, y, z)|)^2} \quad \text{Equation 18}$$

where V is the volume of the simulation, $\rho(x, y, z)$ is the density at a given position, $\mathbf{u}(x, y, z)$ is the displacement field at a given position, and \max_V is the maximum within the volume of the simulation. The zero-point motion of the modes is then calculated, following the equation:

$$x_{ZPM} = \sqrt{\frac{\hbar}{2m_{eff}\Omega_m}} \quad \text{Equation 19}$$

where Ω_m is the angular frequency of eigenmode m . The optomechanical coupling rates are then calculated, following:

$$G = \frac{-2\pi\nu_0}{L_{cavity}} \quad \text{Equation 20}$$

$$g_0 = G \cdot x_{ZPM} \cdot \left(\frac{u_{x,mirror\ 1}}{\max_V (|\mathbf{u}(x, y, z)|)} - \frac{u_{x,mirror\ 2}}{\max_V (|\mathbf{u}(x, y, z)|)} \right) \quad \text{Equation 21}$$

where L_{cavity} is the length of the cavity (here 19 μm), u_x is the maximum displacement in the x direction for an arbitrary perturbation (parallel to the cavity optical axis), and ν_0 is the optical frequency being coupled to.

A linewidth of 1000 Hz ($\Gamma_m = 6283.185$) was used as an approximation for all of the modes, as done in Saavedra *et al* ¹¹. With these linewidths, the frequency noise spectral density can be calculated, following the equation:

$$S_v(f)^2 \approx \frac{2g_0^2}{4\pi^2} \cdot \frac{2\Omega_m}{\hbar} \cdot \frac{2\Gamma_m k_B T}{(\Omega^2 - \Omega_m^2)^2 + \Gamma_m^2 \Omega^2} \quad \text{Equation 22}$$

where Ω is the noise angular frequency ($\Omega = 2\pi f$), temperature is T, and Boltzmann constant is k_B . The critical mode parameters for each mechanical eigenmode are summarized in Table S 4 and the frequency spectrum is plotted in Figure S 14. The frequency noise spectral density for the mechanical motion of the cavity assembly extracted from finite element simulations of the mechanical modes. The resonant mechanical modes lie outside of the velocity-filter bandwidth indicating that the cavity is highly stable within the observation window. The amplitudes of the resonant mechanical modes are below the detector noise limit and are less than the calculated resonance shift for a <1 nm molecule.

Table S 4. Summarized parameters of zero-point mechanical motion of the cavity for the symmetric and antisymmetric mechanical eigenmodes.

Symmetric (S) or Asymmetric (A)	Frequency (MHz)	m_{eff} (Kg)	u_{max} (m)	m_{Norm} (Kg)	Ω_m (MHz)	x_{ZPM} (m)	G (Hzm ⁻¹ /10 ²⁰)	$U_{,x, \text{mirror 1}}$ (m)	$U_{,x, \text{mirror 2}}$ (m)	g_0
S	0.04	1.21E-19	2.24E-08	2.41E-04	0.25	9.30E-19	-1.50	7.15E-09	7.99E-09	5.26E+00
A	0.06	8.25E-20	2.16E-08	1.77E-04	0.37	9.01E-19	-1.50	-2.87E-10	-2.76E-10	6.45E-02
A	0.07	5.31E-20	2.16E-08	1.14E-04	0.45	1.01E-18	-1.50	2.53E-10	2.54E-10	1.33E-02
S	0.09	4.10E-20	2.40E-08	7.12E-05	0.54	1.17E-18	-1.50	1.83E-08	1.88E-08	3.10E+00
A	0.09	3.11E-20	2.17E-08	6.61E-05	0.58	1.18E-18	-1.50	-7.26E-11	-6.08E-11	9.57E-02
S	0.09	3.49E-20	2.63E-08	5.05E-05	0.59	1.33E-18	-1.50	1.58E-08	1.75E-08	1.28E+01
A	0.10	1.12E-20	2.17E-08	2.37E-05	0.61	1.91E-18	-1.50	3.16E-10	3.17E-10	1.38E-02
S	0.10	3.09E-20	2.52E-08	4.88E-05	0.64	1.30E-18	-1.50	9.04E-09	8.81E-09	-1.81E+00
A	0.12	3.26E-21	2.20E-08	6.74E-06	0.75	3.24E-18	-1.50	5.00E-10	5.04E-10	8.66E-02
S	0.14	6.65E-21	2.23E-08	1.34E-05	0.88	2.11E-18	-1.50	3.21E-09	3.51E-09	4.29E+00
A	0.15	2.67E-20	2.20E-08	5.54E-05	0.93	1.01E-18	-1.50	-4.37E-10	-4.41E-10	-3.15E-02
A	0.15	6.66E-21	2.22E-08	1.36E-05	0.94	2.03E-18	-1.50	3.57E-11	4.75E-11	1.63E-01
S	0.16	2.19E-21	2.21E-08	4.45E-06	0.98	3.48E-18	-1.50	2.10E-09	2.18E-09	2.02E+00
S	0.19	6.09E-20	2.58E-08	9.16E-05	1.22	6.86E-19	-1.50	-5.26E-09	-6.13E-09	-3.50E+00

The zero-point motions of the system are calculated to estimate their contribution to the noise experienced by the microcavity as a function of frequency. The noise floor of the

cavity is an order of magnitude lower than the detector noise floor (Supplementary Fig. 14) within the molecular velocity bandwidth. A stepwise integral of S^2 from the locking bandwidth (5 kHz) to the photothermal bandwidth (21 kHz) was calculated, and then the square root taken, giving the integrated noise within the selected region. The RMS resonance shift associated with the integrated noise over the Molecular Velocity Filter Bandwidth is calculated to be approximately 1 kHz, on the same order of magnitude as the resonance shift expected from the smallest molecule, Myc-tag (Table S 2).

Additional Discussion

Navigating Surface Effects in Single-Molecule Studies

Surfaces are ubiquitous in analytical techniques. Simultaneously, a tremendous body of work ¹²⁻¹⁴ has also shown that surfaces induce a variety of conformational changes in biomolecules, ranging from nuanced alterations in dynamics to substantial disruption of secondary and tertiary structures. Different surfaces, from planar glass surfaces to gold nanomaterials, present different mechanisms for surface interactions. Biomolecules at low concentrations, like those most often used in single-molecule studies, often exhibit particularly significant conformational changes. This behavior is attributed to low surface coverage which minimizes the passivation and steric constraints that typically suppress conformational changes observed at higher concentrations ¹². Passivation of surfaces can reduce conformational changes, but the continual presence of defects means that surfaces must always be factored into data interpretation. Molecule-surface interactions are also highly molecule-dependent; with globular proteins displaying a higher resistance to conformational changes, while proteins with more exposed hydrophobic cores are more vulnerable. Disordered proteins are the most susceptible to surface alteration.

Concerns about the impact of surfaces on biomolecular analytes affect the design of sensors and the interpretation of their signals ¹⁴. At one extreme, for label-free single-molecule detection schemes operating as molecular identifiers that rely on antibodies or other

complimentary binders for selectivity^{5,15,16}, the underlying surface may introduce false positive signals through non-specific binding. Nevertheless, the core measurement-whether a molecule has been detected or not- remains inherently reliable. Similarly, for property assessors that are largely agnostic to conformation, such as Mass Photometry¹⁷, the impact of the surface detector is expected to be minimal, though surfaces can sometimes alter quaternary structure^{18,19}. However, for property assessors of conformation and dynamics, there is substantial benefit of minimizing the role of the surface.

The single-molecule fluorescence community has considered this problem and deployed a variety of surface passivation and encapsulation strategies²⁰. However, concerns about the impact of surfaces on dynamics remain, with experiments^{21,22} and simulations²³ having shown differences between surface and solution-phase dynamics. For example, the anti-Brownian electrokinetic (ABEL) trap^{22,24–31} has been deployed for making prolonged single-molecule fluorescence studies away from surfaces, and there have even been attempts to make it label free³². For studies of disordered proteins, a class of molecules highly susceptible to surface-altered conformations, the community standard is to perform measurements on freely diffusing molecules^{25,26,33–36}. Similarly, most practitioners of fluorescence correlation spectroscopy (FCS) perform diffusion constant estimates on molecules somewhat removed from the surface due to contamination of 2D surface dynamics^{37,38}.

In the new area of label-free single-molecule diffusion measurements, two studies deploy strategies to reduce the impact of the proximal surface. Importantly, both of these works are able to measure the hydrodynamic radii of molecules with reasonable accuracy in a label-free manner, albeit with molecules of molecular weight at 60 kDa and greater. In the work of Špačková, Langhammer and co-workers, a “hindrance factor” is included to consider perturbations due to “particle-wall hydrodynamic interactions” inside of a nanofluidic channel³⁹. Further, only negatively charged proteins are examined to minimize sticking to the negatively charged silica surface, while a lipid-passivated nanochannel is used to observe large positively charged lipoprotein particles. In the work of Baaske, Orrit, and co-workers,

molecules are detected as they approach the surface of a plasmonic nanoparticle ⁴⁰. While sticking often occurs, the influence of the surface on the measurement is reduced by examining the rise in signal before the molecule collides with the surface. However, the spatial distribution of the nearfield of the plasmonic particle must be calculated from its physical dimensions in order to determine the diffusion constant. In both cases, charged and potentially time-evolving surfaces may perturb biomolecule behavior and measurement.

Taken together, concerns about how surfaces may impact conformation, diffusion, and molecular dynamics of biomolecules drive the need for truly solution-phase label-free single-molecule studies.

Limitations of our Approach, Context, and Future Directions

Our approach, based on an open-access microcavity with a molecular velocity filter window defined by locking and photothermal bandwidths, represents a new label-free signal transduction mechanism demonstrating the ability to detect single molecules with unparalleled signal-to-noise ratios, and offering insights into diffusive behavior, all while operating at a considerable distance from potentially disruptive surfaces. Despite these exciting advantages, there are also current limitations of the technique that inspire future directions for improvement. While the manuscript has focused on the advantages of the approach, it is crucial to place these limitations within the broader context of the label-free single-molecule techniques ecosystem.

In its current state, while the prominence of the peak is responsible for the conspicuously high signal-to-noise, we derive molecular property information largely from the temporal width of the peak, which was shown to be linear with the molecular radius (Figure 3). Reliance on the temporal width to infer diffusive behavior is a shared feature of the work of Baaske, Orrit, and co-workers ⁴⁰. On the other hand, scattering approaches, including mass photometry ¹⁷ and WGM microresonator approaches without plasmonic enhancement ⁵, are able to relate the intensity of the scattering signal or resonance shift to molecular weight or

polarizability, respectively. In the case of mass photometry, the relationship between signal and molecular weight is particularly straightforward. For detection strategies relying on plasmonic nanoparticles or WGM-plasmonic nanoparticle hybrids, the signal strength is also intimately connected with the angstrom-level structure of the nanoparticle, making the trend more qualitative due to the wide distribution of field strengths at different binding sites ⁴¹. In our system, signal prominence is a non-linear function of molecular parameters (diffusion constant and mass) and system parameters (locking and photothermal bandwidth). Currently, extracting quantitative information from the peak prominence is not feasible. However, development of a detailed model may facilitate this in the future. The system contributes a complex instrument response function, which will require deconvolution from the data. Construction of this model is in progress.

The non-linearity of our signal also introduces challenges to effectively resolve mixtures. Mass photometry ¹⁷ offers both precision and high dynamic range for molecular weight that can be deployed to resolve complex mixtures. When combined with use of nanofluidics ³⁹, long particle trajectories confer the ability to resolve simple mixtures according to hydrodynamic radius. While our method can resolve binary mixtures, including isomers of the same, small, molecular weight, resolution of a ternary mixture (Extended Data Fig. 7) appears to be just at the edge of feasibility (see **“Error! Reference source not found.”** section above). Part of this current limitation appears to evolve from some degree of mode wandering, which broadens the prominence histograms. However, this is not a fundamental limitation, and this issue will likely be resolved with improvements in engineering. Nevertheless, the non-linearity of our response suggests that resolution of highly complex mixtures with a single set of parameters is likely not possible due to the finite dynamic range. Alternatively, systematically adjusting system parameters can shift different molecules in and out of that dynamic range. We are currently testing this strategy to enhance precision, expand the dynamic range, and assess the resolution capabilities for complex mixtures. We note many key biotechnological applications can result from, for example, resolving a small number of

components in a simple, even binary mixture, such as a drug binding to a pharmaceutical target.

Another limitation concerns concentration. Samples are prepared in the 0.25-15 pM range. This low concentration range is a consequence of both the high sensitivity and high “capture volume” of our approach where a large fraction of the mode volume, a micro-sized volume rather than a nano-sized volume, is capable of revealing a single molecule. On one hand, this low concentration range is beneficial for being able to yield robust signals with extremely small amounts of material and may be a benefit for examining biomarkers that are present in the blood at fM concentrations, or for single molecules that are capable of initiating cellular responses in the picomolar and sub-picomolar range ⁴². On the other hand, quaternary structure of biomolecules, or the binding of biomolecules to small molecules, may be destabilized under these conditions. Use of smaller mode volume microcavities, such as fiber mirrors with more extreme radii of curvature, could potentially increase this range by one or two orders of magnitude, but at the cost of more interaction with surfaces. Still, this low concentration range is likely an inherent feature of our approach. One way to resolve this issue is to couple the microcavity to a microfluidic infrastructure, as has been done by Hunger and co-workers ⁴, and deploy rapid mixing approaches to examine biomolecular superstructure before they disassemble.

A further limitation of the approach derives from its confocal nature, where only a single molecule is examined at a time. In contrast, interferometric scattering-based methods offer a widefield capability,¹⁷ allowing the simultaneous probing of many molecules, and the extended observation of one molecule over time. This feature is used highly effectively in combination with nanofluidics ³⁹ to extract diffusion constants from long molecular trajectories. The ability to repeatedly sample the same molecule would allow a substantial increase in precision in molecular property assessment. As our approach relies on Brownian motion, the same molecule may exhibit different temporal peak shapes as it stochastically explores the mode volume. Repeated sampling of the same molecule, as is already likely happening in some of the “clustered” peaks in our data set, would allow us to average many trajectories over the

same molecule. The use of coupled microfluidics could also allow this process to be controllably engineered, with similar geometries already being used to direct molecular position in fluorescence-based systems^{22,25,26}.

There are other experimental limitations that are certainly not fundamental and will be addressed with more robust and mature engineering and calibration procedures. As mentioned above, cavity mode wandering is a nuisance that can likely be addressed with new mounting procedures. We have also seen some evidence of microcavity fouling, observed as an increase in the photothermal responsivity of the microcavity, eventually to the point of making the cavity unstable. Fouling was noticed to be slower for nucleic acids than for proteins, suggesting a photochemical surface interaction. This issue can also be addressed with improved cleaning procedures. Quantitative comparisons of data acquired in different microcavities is difficult due to the non-linear measurement's sensitivity to quality factor, photothermal nonlinearity, and variations in the optical mode, which all change from microcavity to microcavity. This issue can be addressed by developing a calibration process, a common requirement for molecular analytical tools.

Supplementary Figures and Tables

Table S 5. Parameters of the cavities used in this work. The cavities used to collect the data shown in the figures of the main text are indicated in this table, the cavities used to collect the data shown in the supplementary figures are indicated in the respective figure legends.

Parameter	Cavity one	Cavity two	Cavity three	Cavity four
λ_{pump} (nm)	660	660	660	760
Finesse	37450	17909	21780	30000
Cavity length (μm)	19	19	24	20
$\Delta\nu$ (MHz)	206.87	398.83	286.9	261
ROC mirror 1 (μm)	122.4	116.9	60.9	$\sim 170 \mu\text{m}$
ROC mirror 2 (μm)	97.7	105.5	67.5	$\sim 170 \mu\text{m}$
Figure 1	X			
Figure 2	X			
Figure 3	X			
Figure 4		X		
Figure 5				X

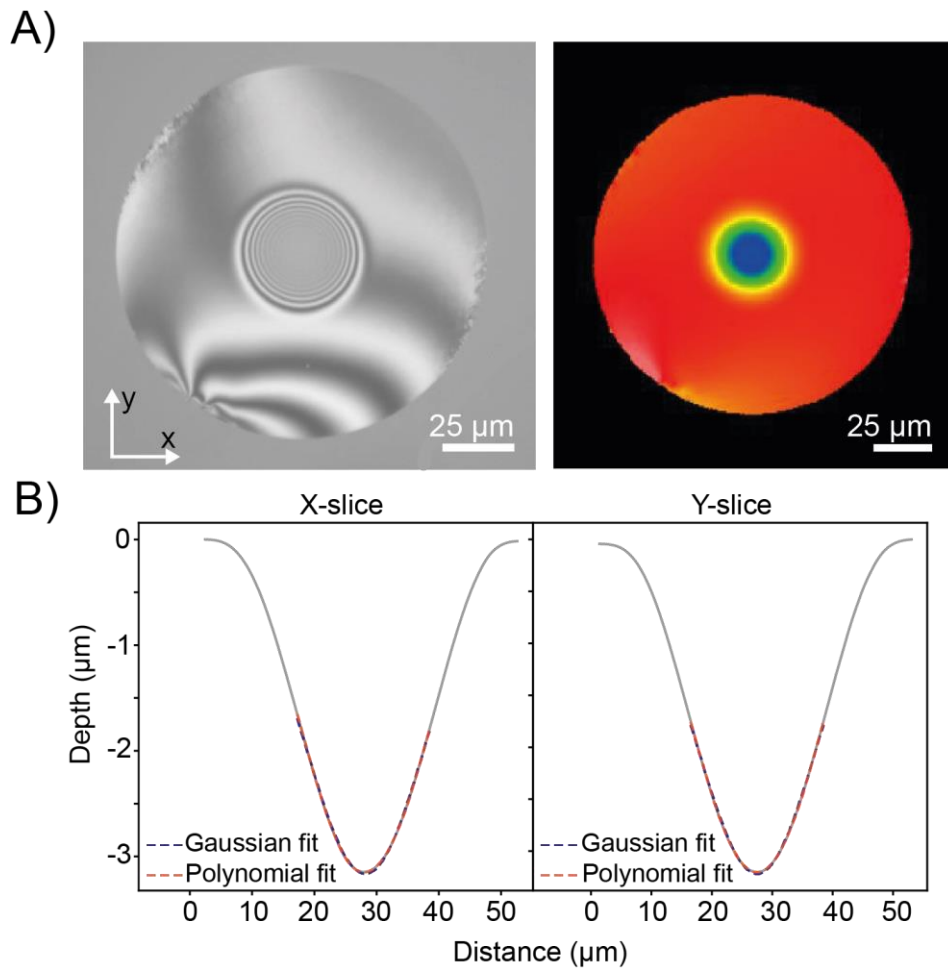


Figure S 1. A) Interferometry profiles of the concave depression created by CO₂ laser ablation into the face of an optical fiber. **B)** Resulting 2D depth profiles created from X and Y slices of the interferometry images, these are fitted with appropriate functions to define the radius of curvature (ROC) and diameter of the ablation.

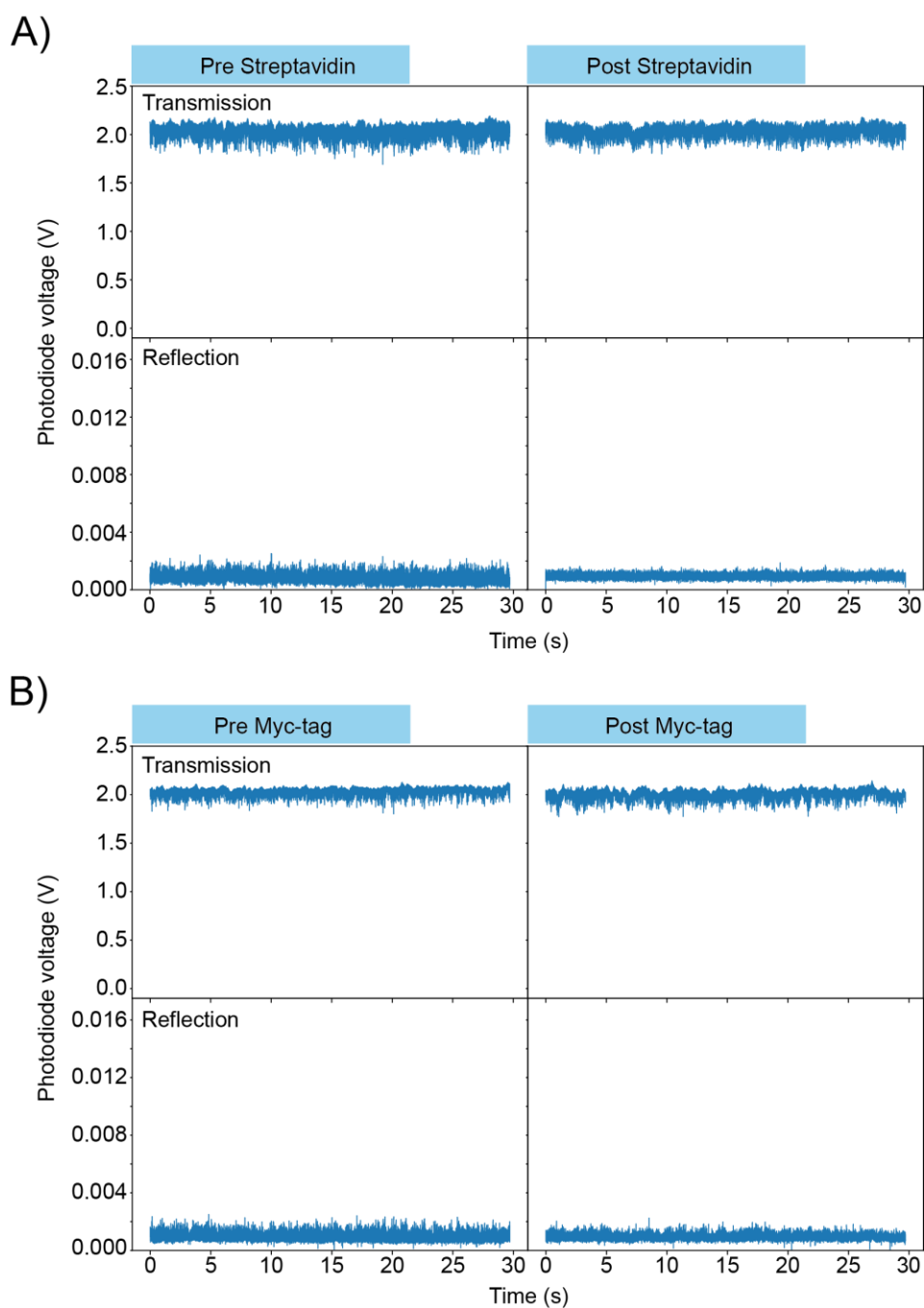


Figure S 2. Representative intensity vs time traces of a locked water filled cavity in the absence of molecules in both transmission and reflection either **A)** pre and post introduction of streptavidin or **B)** pre and post introduction of Myc-tag. The lack of signal here demonstrates that the transient perturbations (Fig 2A) originate from molecules. Data collected in cavity one.

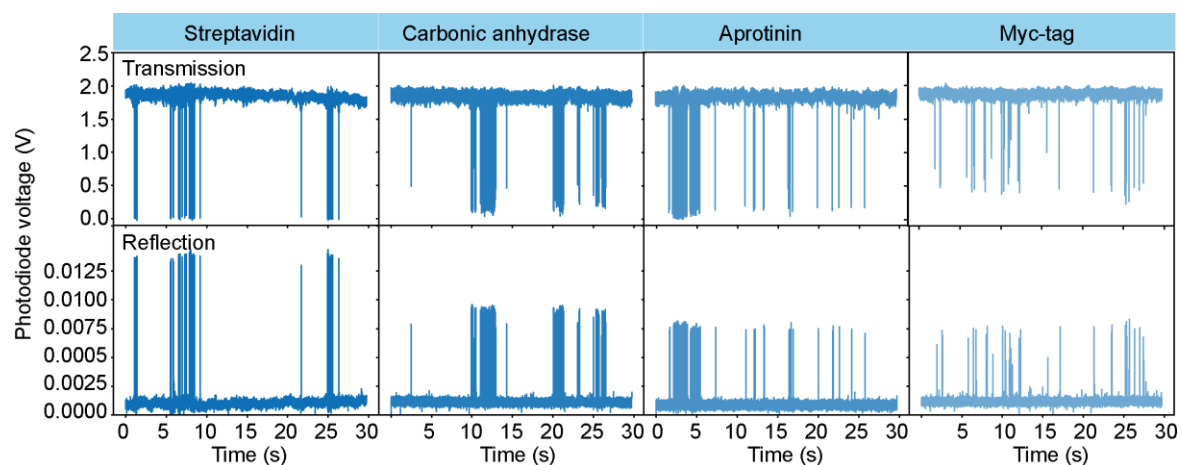


Figure S 3. Full 30 s time traces of protein data displayed in Figure 2A in the Main Text. Data collected in cavity one.

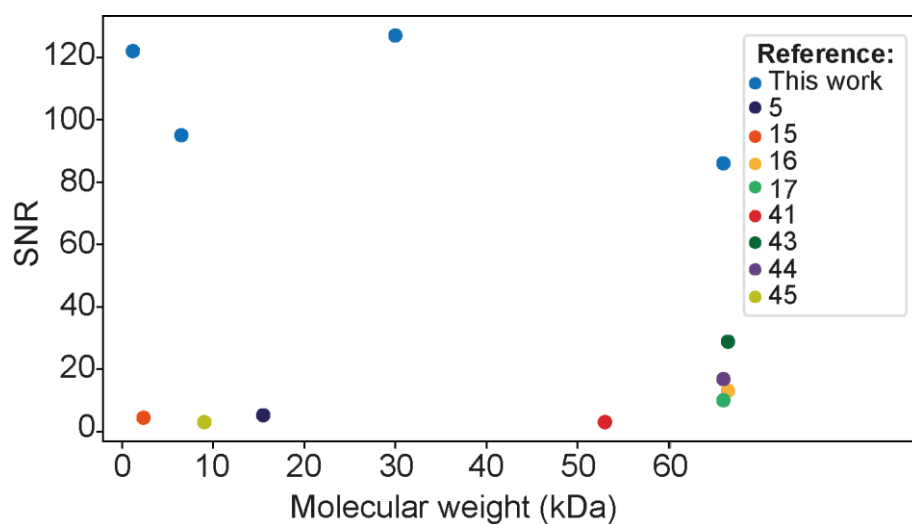


Figure S 4. Comparison between signal to noise ratios of this work and other label-free, single-molecule studies ^{5,15–17,41,43–45}. Single-molecule diffusion data shown in Fig 2A and collected in cavity one.

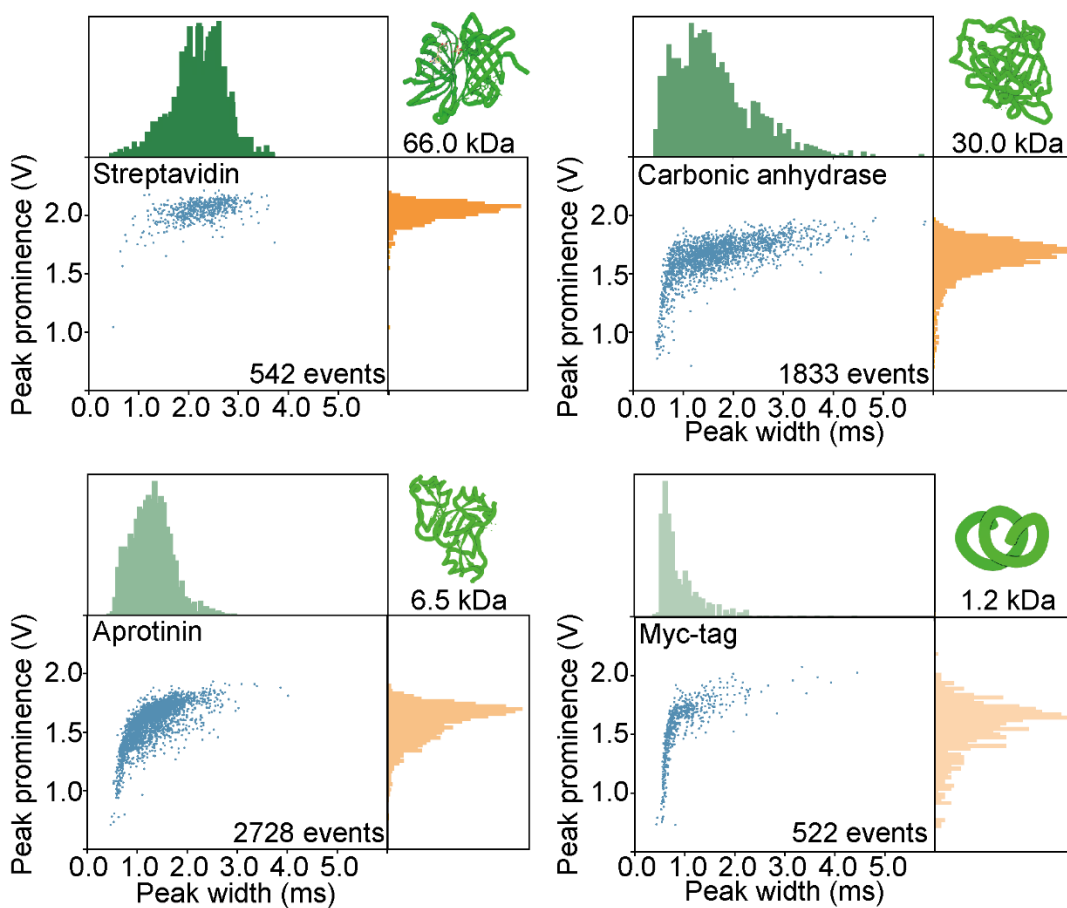


Figure S 5. 2D plots and accompanied histograms of the extracted prominences and temporal widths of the transmitted signals. The reflection signals are displayed in Figure 2A in the main text. Data collected in cavity one.

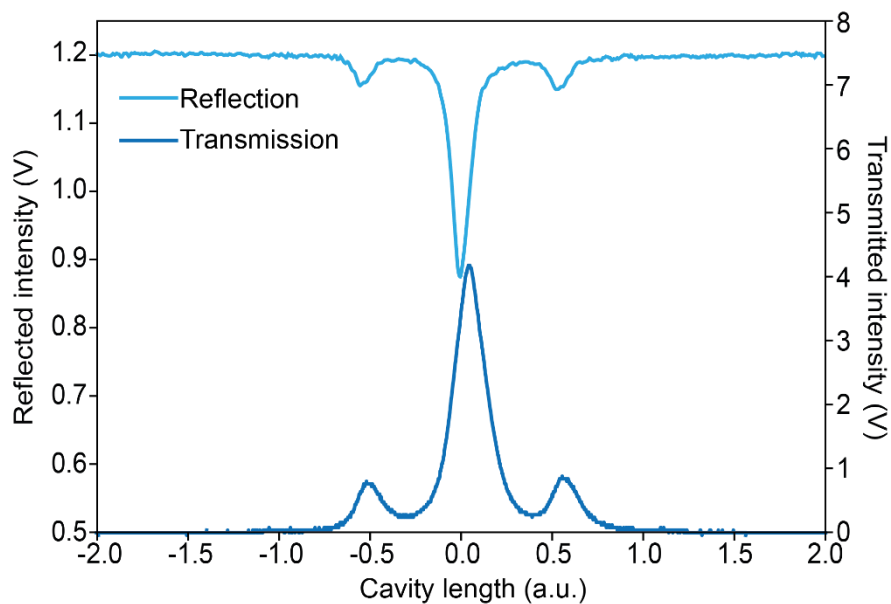


Figure S 6. Example resonances in reflection and transmission under cavity length translation. The frequency of the reflected signal is offset relative to the transmitted signal by 309 MHz due to mode matching leading to dispersion. Data collected with cavity one.

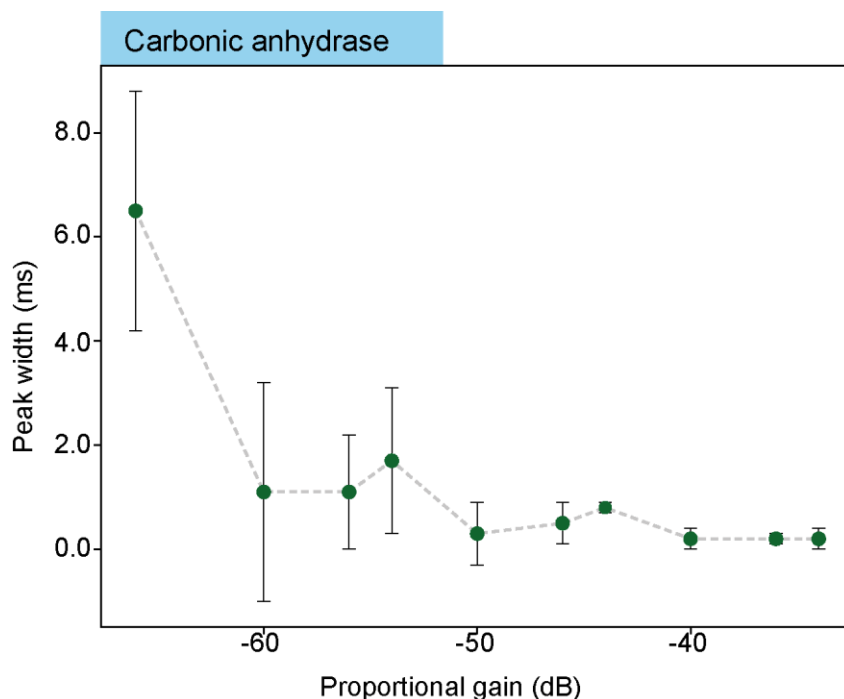


Figure S 7. Temporal widths of carbonic anhydrase diffusion events as a function of the locking bandwidth of the PDH determined by the proportional gain of the PI control. This relationship can be explained by the inverse relationship between the molecular velocity filter bandwidth and the proportional gain values. As the gain is increased the velocity filter bandwidth narrows, resulting in detection of a distribution of faster moving molecules with narrower peak widths. Data was collected at proportional gain settings >-50 dB where the mean temporal width was no longer influenced by the locking bandwidth. Error bars represent the standard deviation of temporal widths across all analyzed peaks. Data collected with cavity three.

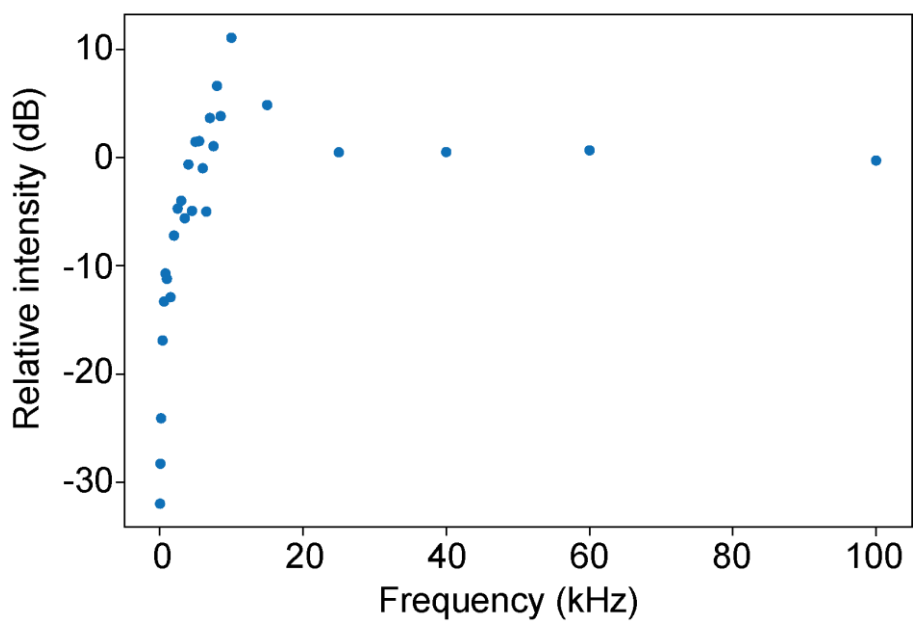


Figure S 8. Determination of the locking bandwidth. The frequency of the locking bandwidth is determined at the relative intensity crossing at 0 dB and is approximately 5 kHz. Data collected with cavity two.

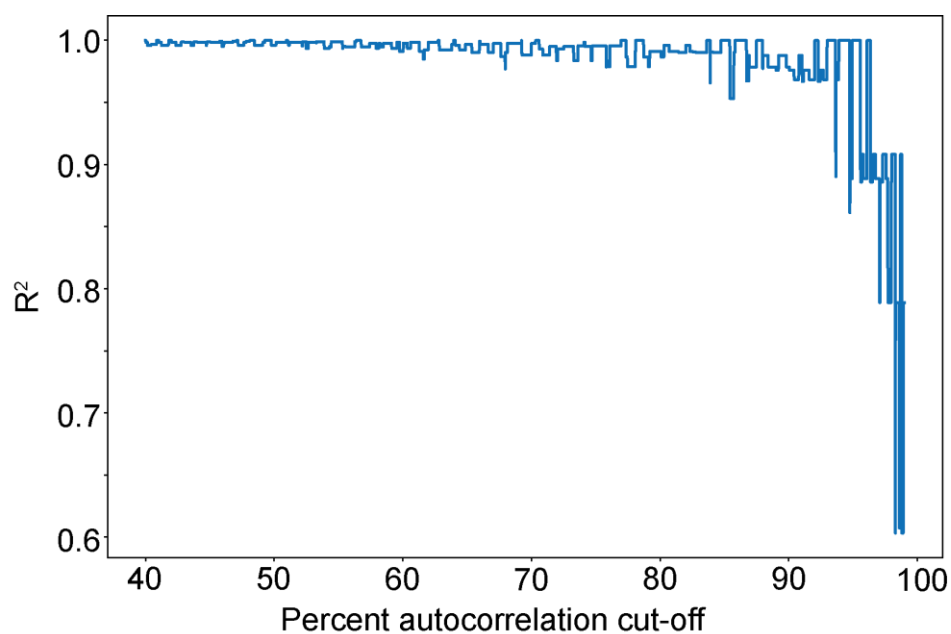


Figure S 9. Linearity of the autocorrelation function as a function of protein radius measured via the R^2 of the linear fit versus the percentage autocorrelation cut-off shown in Figure 3 in the main text. R^2 is the coefficient of determination and is a statistical measure of how well the data fits to a linear model. This

linear trend was clearly preserved for a large range of decay values, demonstrating the robustness of the analysis.

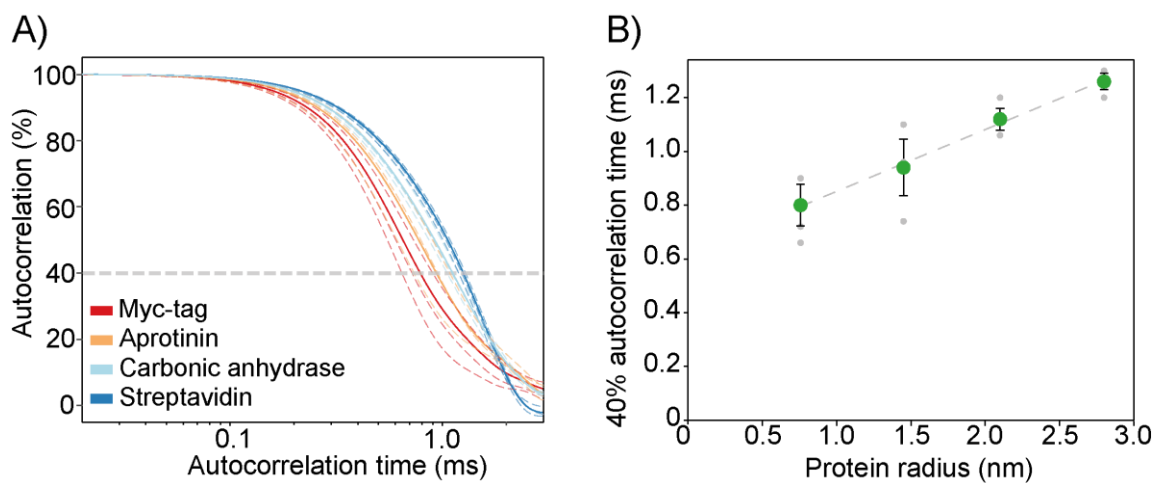


Figure S 10. A) Ensemble autocorrelation of several hundred single-protein diffusion events with same data as shown in Fig 3. The solid curves represent the full autocorrelation across all replicates and the dashed curves represent individual replicates. **B)** Same as Figure 3b, relationship between mean autocorrelation time at an autocorrelation threshold of 40% and the protein radius, showing the linear correlation, but with extended axes to show non-zero intercept due to finite response of the photothermal mechanism. The error bars represent the standard deviation from three experiments within the same cavity.

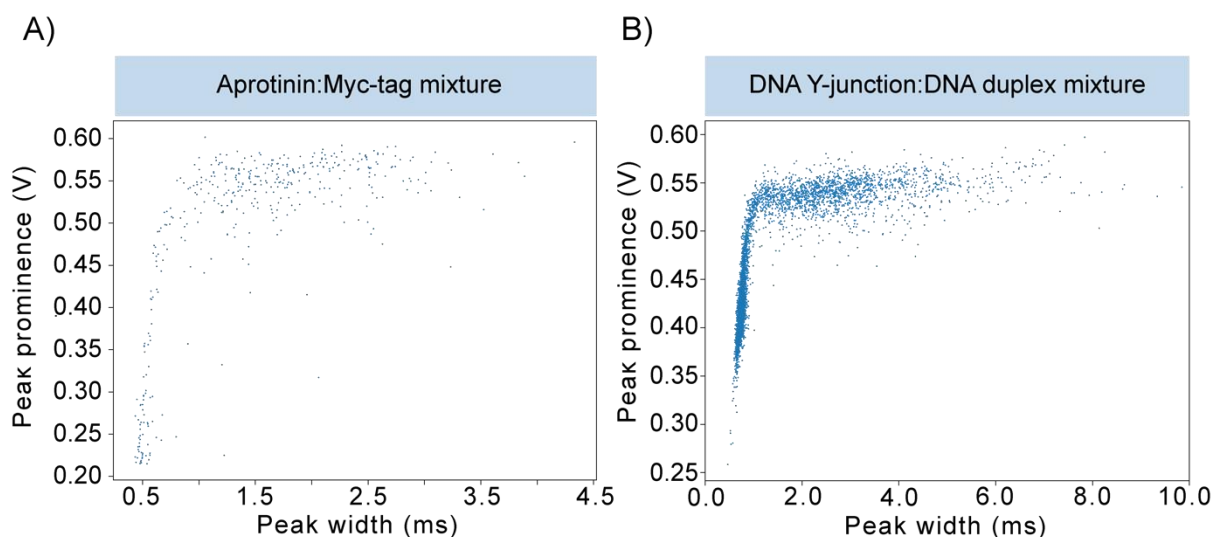


Figure S 11. Corresponding scatter plots of the contour plots in shown In Figure 4 for **A)** a binary mixture of Aprotinin and Myc-tag and **B)** a binary mixture of a DNA Y-junction and duplex (Table S 1).

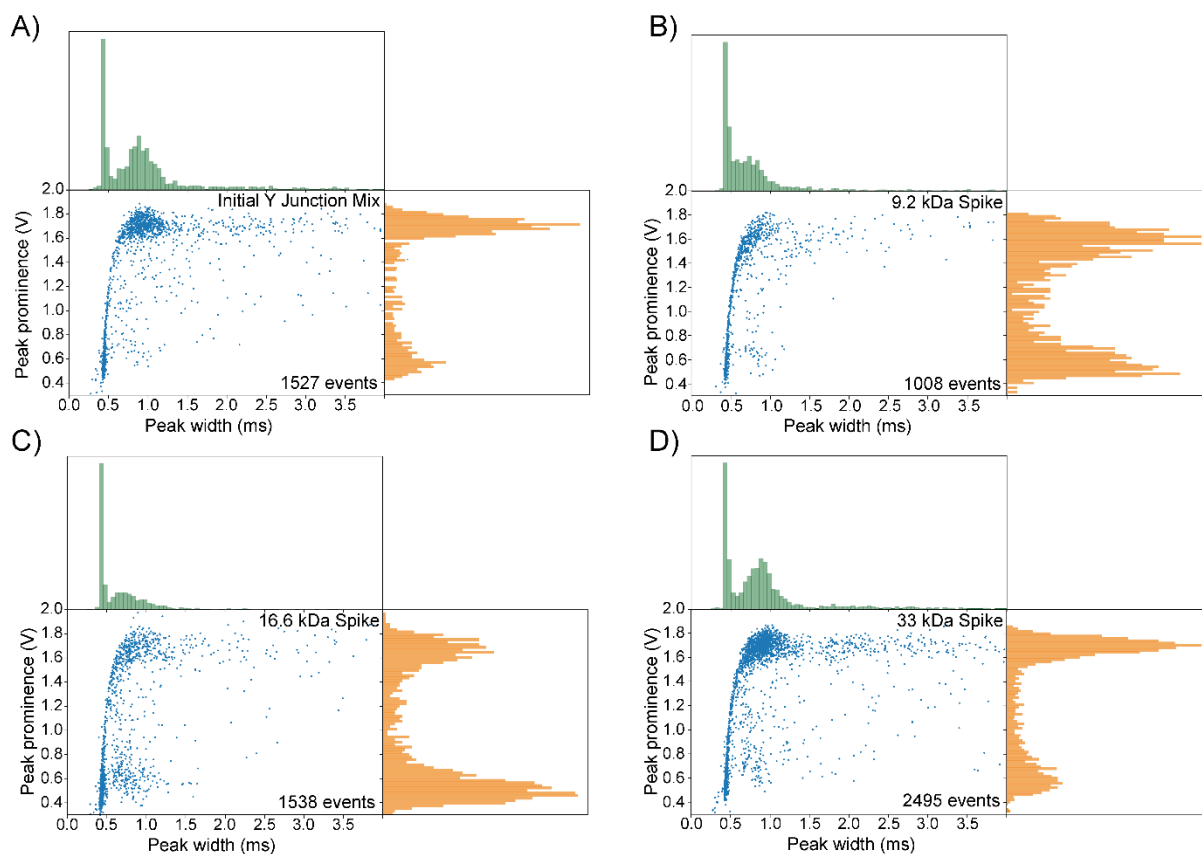


Figure S 12. 2D scatter plots and accompanied histograms of the extracted prominences and temporal widths of the transmitted signals from a ternary mixture of DNA Y-junction molecules (Table S 1) of differing mass for **A)** an equimolar mixture, **B)** spiked 9.2 kDa Y-junction, **C)** spiked 16.6 kDa Y-junction and **D)** spiked 33.3 kDa Y-junction

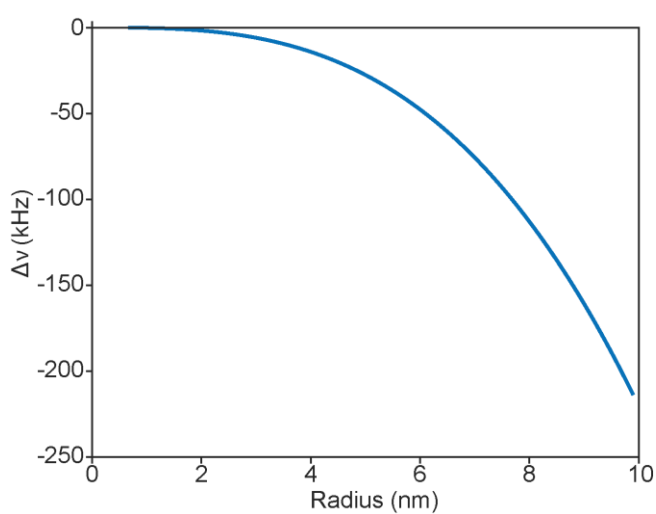


Figure S 13. Analytical calculation of the resonance frequency shift induced by objects of refractive index=1.43 for radii <10 nm.

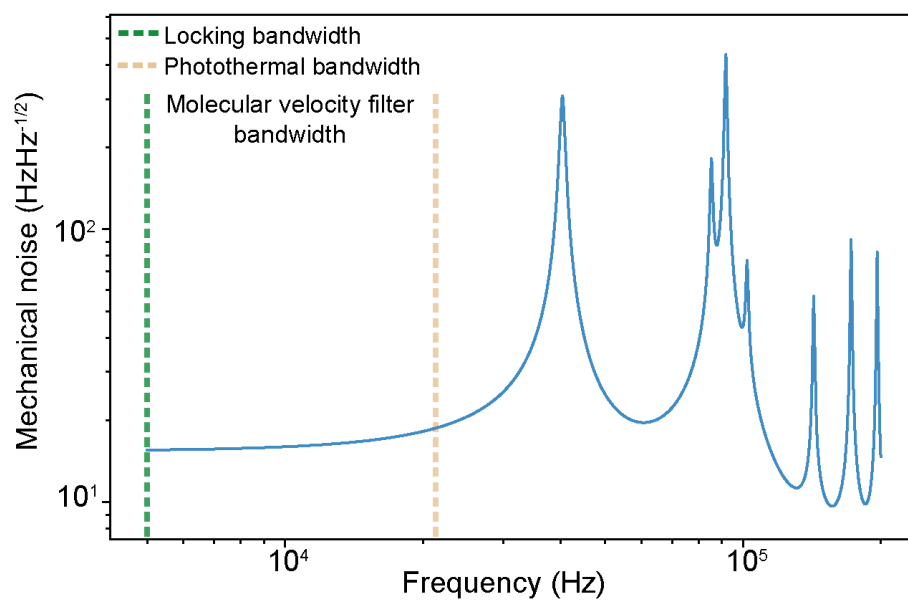


Figure S 14. The frequency noise spectral density for the mechanical motion of the cavity assembly extracted from finite element simulations of the mechanical modes. The resonant mechanical modes lie outside of the velocity-filter bandwidth indicating that the cavity is highly stable within the observation window. The amplitudes of the resonant mechanical modes are below the detector noise limit and are less than the calculated resonance shift for a <1 nm molecule.

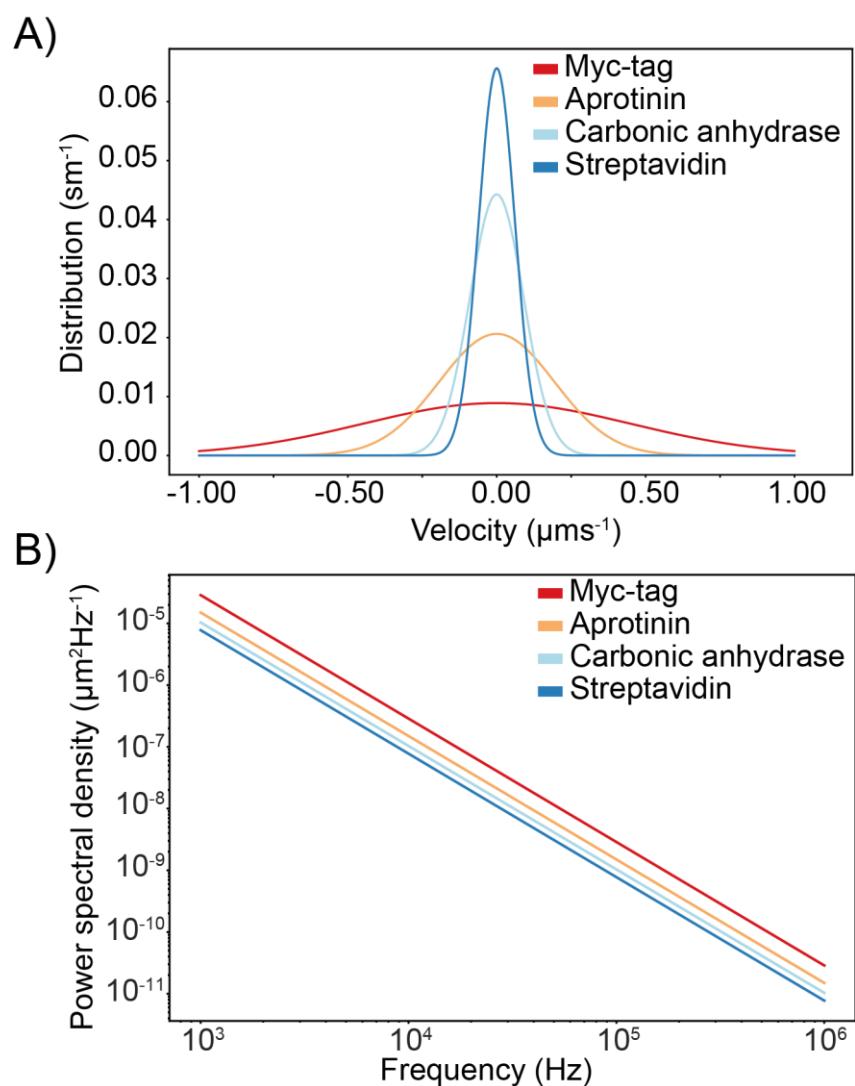


Figure S 15 A) Calculated velocity distribution profiles for Myc-tag, aprotinin, carbonic anhydrase and streptavidin **B)** Mean-square-displacement power spectral density plot (MSDPSD), the upper and lower bounds are replicated in the main text, Fig 5A. Integrating within the bandwidth of our velocity filter observation window (5 kHz-150 kHz) provides an approximate MSD for the molecule.

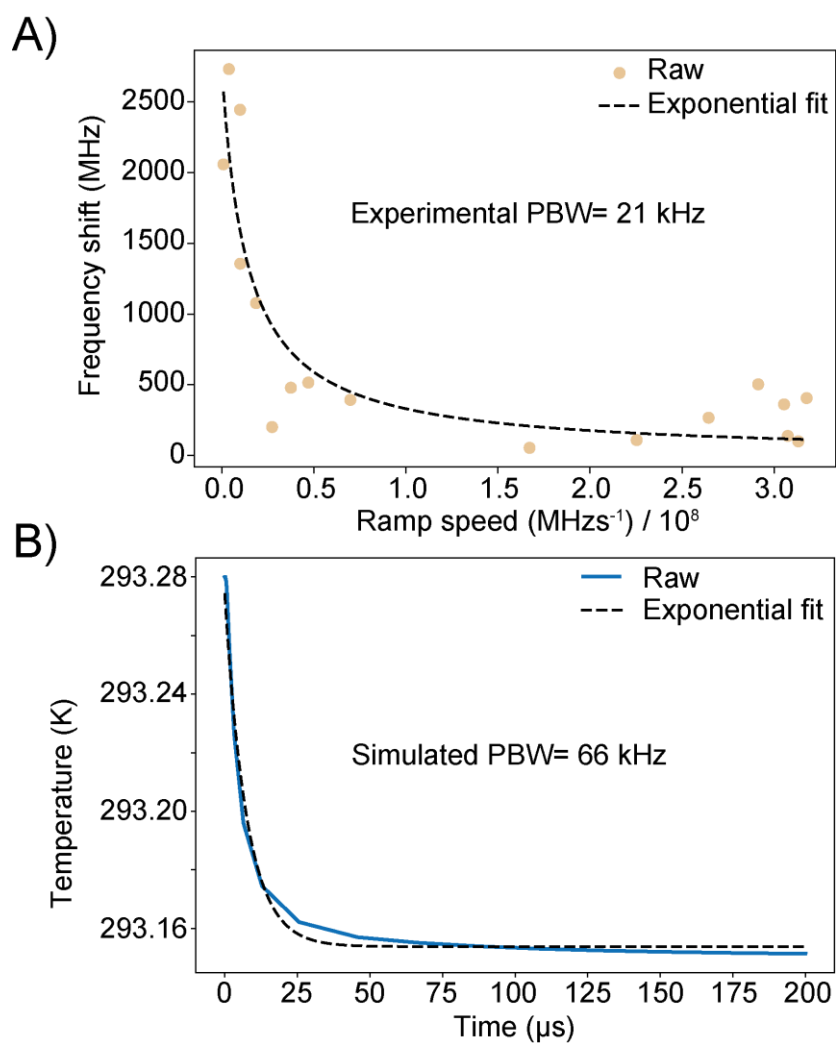


Figure S 16. A) Experimental determination of the photothermal bandwidth (PBW). The calculated bandwidth is 21 kHz, defining the upper limit of the molecular velocity filter (data collected with cavity four). As a comparison, **B)** finite element simulations of the rate of cooling in the cavity were performed to theoretically quantify the PBW

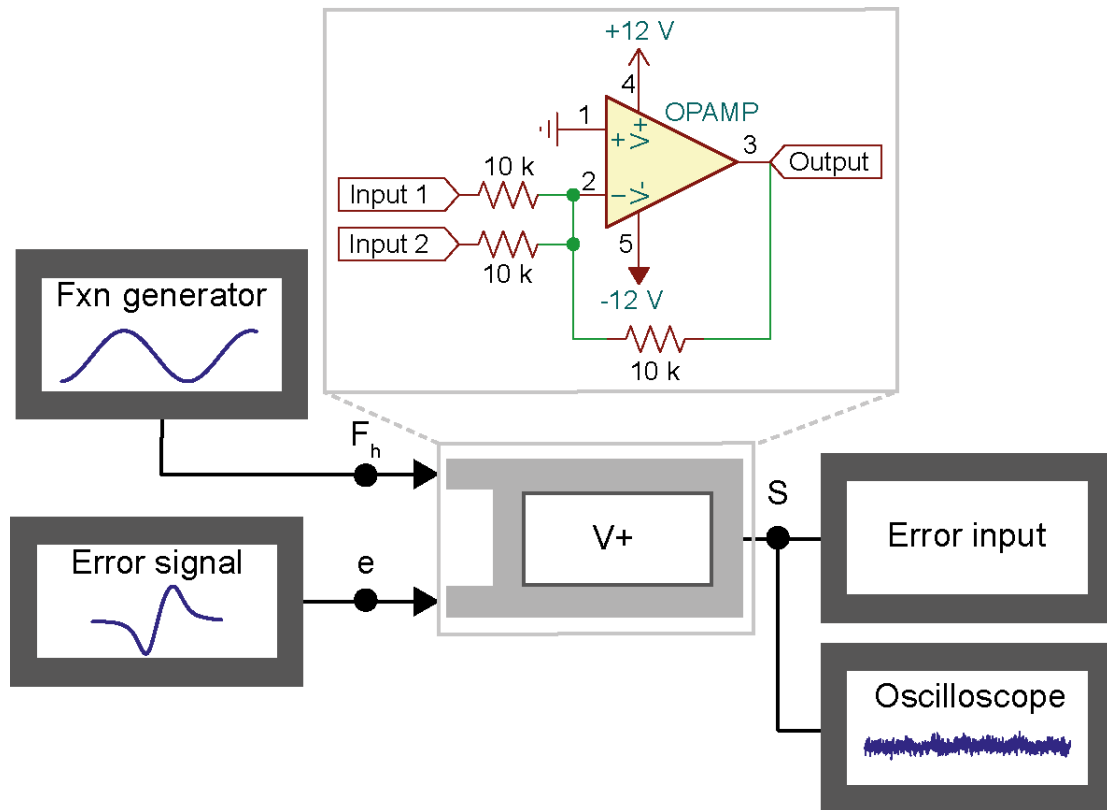


Figure S 17. Schematic of the apparatus used to measure the locking bandwidth of the cavity, which was measured by adding a harmonic perturbation (F_h) from the function generator (Fxn generator) of known frequency and amplitude together with the error signal (e) using an inverting voltage adder ($V+$) to the PI input (error input).

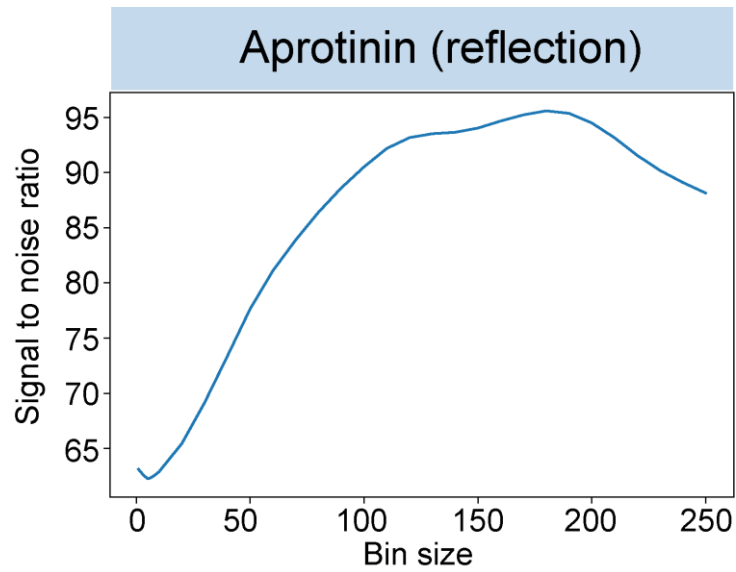


Figure S 18. Signal-to-noise-ratios for Aprotinin as a function of moving average bin size.

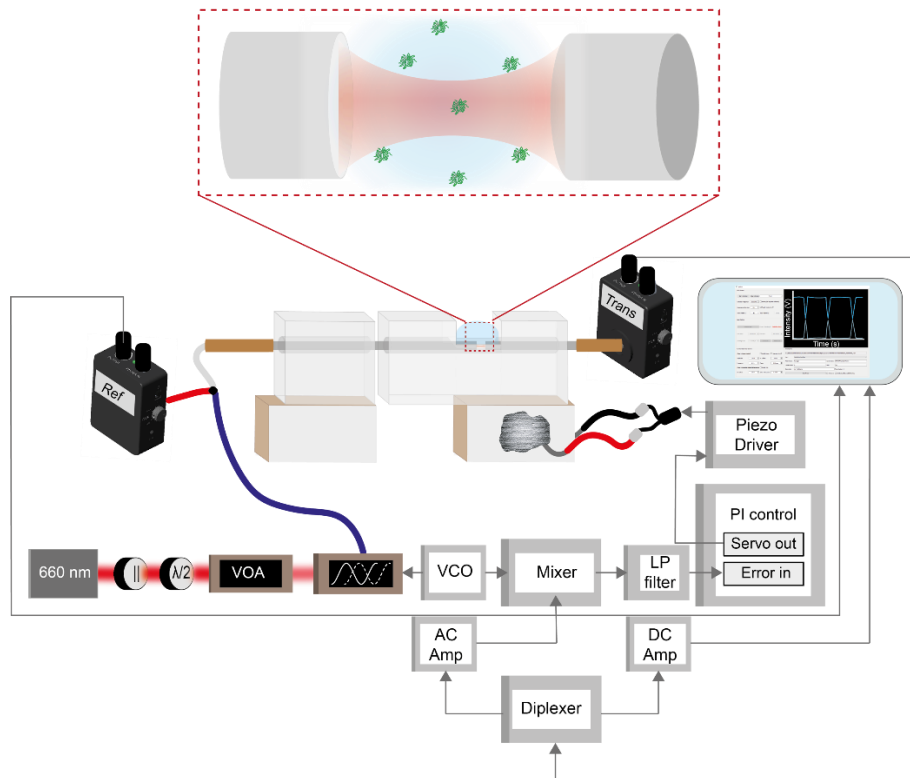


Figure S 19. Complete diagram showing the optical and electronic components of the setup, described in detail in Methods.

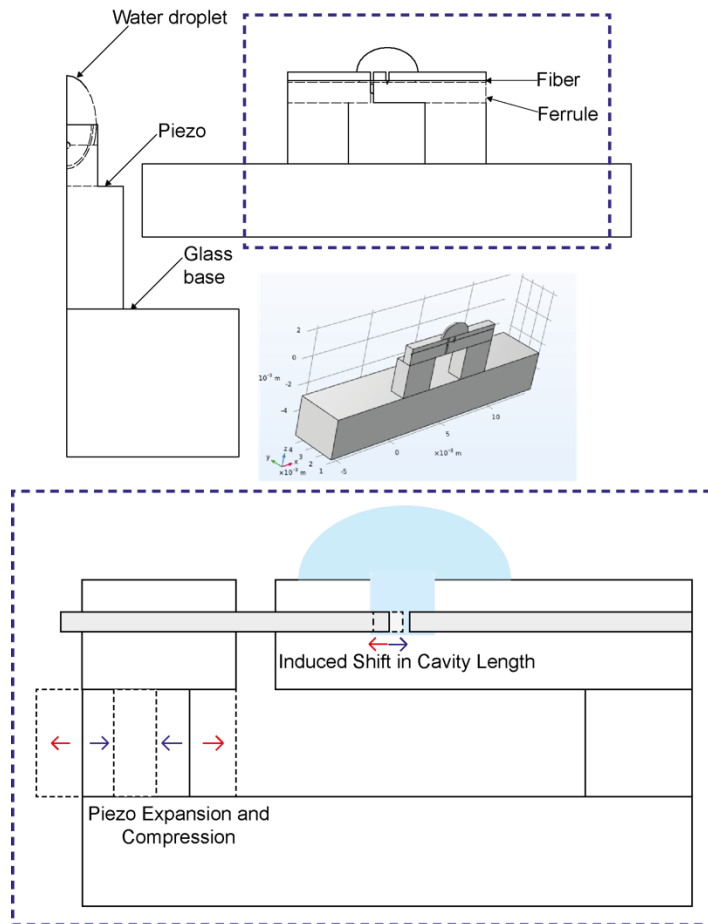


Figure S 20. Schematic of the cavity assembly model used for fiber mechanics COMSOL simulations.

Supplementary references

1. Bethe, A. H. & Schwinger, J. *Perturbation Theory for Cavities*. (Massachusetts Institute of Technology, Radiation Laboratory, 1943).
2. Yu, D. *et al.* Whispering-gallery-mode sensors for biological and physical sensing. *Nature Reviews Methods Primers* vol. 1 Preprint at <https://doi.org/10.1038/s43586-021-00079-2> (2021).
3. Arnold, S., Shopova, S. I. & Holler, S. Whispering gallery mode bio-sensor for label-free detection of single molecules: thermo-optic vs. reactive mechanism. *Opt Express* **18**, 281–287 (2010).
4. Kohler, L., Mader, M., Kern, C., Wegener, M. & Hunger, D. Tracking Brownian motion in three dimensions and characterization of individual nanoparticles using a fiber-based high-finesse microcavity. *Nat Commun* **12**, 1–7 (2021).
5. Su, J., Goldberg, A. F. & Stoltz, B. M. Label-free detection of single nanoparticles and biological molecules using microtoroid optical resonators. *Light Sci Appl* **5**, 1–6 (2016).
6. Mo, J., Simha, A., Kheifets, S. & Raizen, M. G. Testing the Maxwell-Boltzmann distribution using Brownian particles. *Opt Express* **23**, 1888 (2015).
7. Carmon, T., Yang, L. & Vahala, K. J. Dynamical thermal behavior and thermal self-stability of microcavities. *Opt Express* **12**, 4742–4750 (2004).
8. Gallego, J. *et al.* High-finesse fiber Fabry–Perot cavities: stabilization and mode matching analysis. *Applied Physics B* **122**, 47 (2016).
9. Demtröder, W. *Laser Spectroscopy 1. Laser Spectroscopy 1: Basic Principles* (Springer Berlin Heidelberg, Berlin, Heidelberg, 2014). doi:10.1007/978-3-642-53859-9.
10. Casset, F. *et al.* Young modulus and Poisson ratio of PZT thin film by Picosecond Ultrasonics. *IEEE International Ultrasonics Symposium, IUS* 2180–2183 (2012) doi:10.1109/ULTSYM.2012.0544.

11. Saavedra, C., Pandey, D., Alt, W., Pfeifer, H. & Meschede, D. Tunable fiber Fabry-Perot cavities with high passive stability. *Opt Express* **29**, 974 (2021).
12. Yano, Y. F. Kinetics of protein unfolding at interfaces. *Journal of Physics Condensed Matter* vol. 24 Preprint at <https://doi.org/10.1088/0953-8984/24/50/503101> (2012).
13. Faulón Marruecos, D., Schwartz, D. K. & Kaar, J. L. Impact of surface interactions on protein conformation. *Current Opinion in Colloid and Interface Science* vol. 38 Preprint at <https://doi.org/10.1016/j.cocis.2018.08.002> (2018).
14. Frutiger, A. *et al.* Nonspecific Binding - Fundamental Concepts and Consequences for Biosensing Applications. *Chemical Reviews* vol. 121 Preprint at <https://doi.org/10.1021/acs.chemrev.1c00044> (2021).
15. Baaske, M. D., Foreman, M. R. & Vollmer, F. Single-molecule nucleic acid interactions monitored on a label-free microcavity biosensor platform. *Nat Nanotechnol* **9**, 933–939 (2014).
16. Dantham, V. R. *et al.* Label-free detection of single protein using a nanoplasmonic-photonic hybrid microcavity. *Nano Lett* **13**, 3347–3351 (2013).
17. Young, G. *et al.* Quantitative mass imaging of single biological macromolecules. *Science* **360**, 423–427 (2018).
18. Rabe, M., Verdes, D. & Seeger, S. Understanding protein adsorption phenomena at solid surfaces. *Advances in Colloid and Interface Science* vol. 162 Preprint at <https://doi.org/10.1016/j.cis.2010.12.007> (2011).
19. Tarasevich, B. J., Lea, S., Bernt, W., Engelhard, M. H. & Shaw, W. J. Changes in the quaternary structure of amelogenin when adsorbed onto surfaces. *Biopolymers* **91**, (2009).
20. Rasnik, I., McKinney, S. A. & Ha, T. Surfaces and Orientations: Much to FRET about? *Acc Chem Res* **38**, (2005).
21. Talaga, D. S. *et al.* Dynamics and folding of single two-stranded coiled-coil peptides studied by fluorescent energy transfer confocal microscopy. *Proc Natl Acad Sci U S A* **97**, (2000).

22. Goldsmith, R. H. & Moerner, W. E. Watching conformational- and photodynamics of single fluorescent proteins in solution. *Nature Chemistry* **2010** 2:3 **2**, 179–186 (2010).
23. Friedel, M., Baumketner, A. & Shea, J.-E. Effects of surface tethering on protein folding mechanisms. *Proceedings of the National Academy of Sciences* **103**, 8396–8401 (2006).
24. Wang, Q., Goldsmith, R. H., Jiang, Y., Bockenhauer, S. D. & Moerner, W. E. Probing Single Biomolecules in Solution Using the Anti-Brownian Electrokinetic (ABEL) Trap. *Acc Chem Res* **45**, 1955–1964 (2012).
25. Foote, A. K., Manger, L. H., Holden, M. R., Margittai, M. & Goldsmith, R. H. Time-resolved multirotational dynamics of single solution-phase tau proteins reveals details of conformational variation. *Physical Chemistry Chemical Physics* **21**, (2019).
26. Manger, L. H. *et al.* Revealing Conformational Variants of Solution-Phase Intrinsically Disordered Tau Protein at the Single-Molecule Level. *Angewandte Chemie - International Edition* **56**, 15584–15588 (2017).
27. Wang, Q. & Moerner, W. E. Single-molecule motions enable direct visualization of biomolecular interactions in solution. *Nat Methods* **11**, 555–558 (2014).
28. Yang, H. Y. & Moerner, W. E. Resolving Mixtures in Solution by Single-Molecule Rotational Diffusivity. *Nano Lett* **18**, (2018).
29. Fields, A. P. & Cohen, A. E. A Flexible Anti-Brownian Electrokinetic (ABEL) Trap for Single-Molecule Immobilization in Solution. *Biophys J* **96**, (2009).
30. Squires, A. H. & Moerner, W. E. Direct single-molecule measurements of phycocyanobilin photophysics in monomeric C-phycocyanin. *Proc Natl Acad Sci U S A* **114**, (2017).
31. Dienerowitz, M., Howard, J. A. L., Quinn, S. D., Dienerowitz, F. & Leake, M. C. Single-molecule FRET dynamics of molecular motors in an ABEL trap. *Methods* **193**, (2021).
32. Squires, A. H., Lavania, A. A., Dahlberg, P. D. & Moerner, W. E. Interferometric Scattering Enables Fluorescence-Free Electrokinetic Trapping of Single Nanoparticles in Free Solution. *Nano Lett* **19**, (2019).

33. Aznauryan, M., Nettels, D., Holla, A., Hofmann, H. & Schuler, B. Single-molecule spectroscopy of cold denaturation and the temperature-induced collapse of unfolded proteins. *J Am Chem Soc* **135**, (2013).
34. Banerjee, P. R., Mitrea, D. M., Kriwacki, R. W. & Deniz, A. A. Asymmetric Modulation of Protein Order-Disorder Transitions by Phosphorylation and Partner Binding. *Angewandte Chemie - International Edition* **55**, (2016).
35. Elbaum-Garfinkle, S. & Rhoades, E. Identification of an aggregation-prone structure of tau. *J Am Chem Soc* **134**, (2012).
36. Mao, A. H., Crick, S. L., Vitalis, A., Chicoine, C. L. & Pappu, R. V. Net charge per residue modulates conformational ensembles of intrinsically disordered proteins. *Proc Natl Acad Sci U S A* **107**, (2010).
37. Mahurin, S. M., Dai, S. & Barnes, M. D. Probing the diffusion of a dilute dye solution in mesoporous glass with fluorescence correlation spectroscopy. *Journal of Physical Chemistry B* **107**, (2003).
38. Lyon, W. A. & Nie, S. Confinement and Detection of Single Molecules in Submicrometer Channels. *Anal Chem* **69**, (1997).
39. Špačková, B. *et al.* Label-free nanofluidic scattering microscopy of size and mass of single diffusing molecules and nanoparticles. *Nat Methods* **19**, (2022).
40. Baaske, M. D., Asgari, N., Punj, D. & Orrit, M. Nanosecond time scale transient optoplasmonic detection of single proteins. *Sci Adv* **8**, 5576 (2022).
41. Zijlstra, P., Paulo, P. M. R. & Orrit, M. Optical detection of single non-absorbing molecules using the surface plasmon resonance of a gold nanorod. *Nat Nanotechnol* **7**, 379–382 (2012).
42. Civciristov, S. & Halls, M. L. Signalling in response to sub-picomolar concentrations of active compounds: Pushing the boundaries of GPCR sensitivity. *British Journal of Pharmacology* vol. 176 Preprint at <https://doi.org/10.1111/bph.14636> (2019).

43. Mauranyapin, N. P., Madsen, L. S., Taylor, M. A., Waleed, M. & Bowen, W. P. Evanescent single-molecule biosensing with quantum-limited precision. *Nat Photonics* **11**, 477–481 (2017).
44. Yu, W., Jiang, W. C., Lin, Q. & Lu, T. Cavity optomechanical spring sensing of single molecules. *Nat Commun* **7**, 12311 (2016).
45. Dahmardeh, M., Mirzaalian Dastjerdi, H., Mazal, H., Köstler, H. & Sandoghdar, V. Self-supervised machine learning pushes the sensitivity limit in label-free detection of single proteins below 10 kDa. *Nat Methods* **20**, 442–447 (2023).